A neural field model for ignition and propagation of cortical spreading depression

E Baspinar, D Avitabile, M Desroches, M Mantegazza

A neural field model for ignition and propagation of cortical spreading depression

E. Baspinar[1,*], D. Avitabile[2,3,4], M. Desroches[4], M. Mantegazza[5,6,7]

[1]CNRS, Paris-Saclay University, Institute of Neuroscience (NeuroPSI), Saclay, France

[2]Department of Mathematics, Vrije Universiteit Amsterdam, Amsterdam, The Netherlands

[3]Amsterdam Neuroscience - System and Network Neuroscience

[4]MathNeuro Team, Inria Center at Université Côte d'Azur, Sophia Antipolis, France

[5]Université Côte d'Azur, Institute of Molecular and Cellular Pharmacology (IPMC), Valbonne-Sophia Antipolis, France.

[6]CNRS UMR7275, Institute of Molecular and Cellular Pharmacology (IPMC), Valbonne-Sophia Antipolis, France.

[7]INSERM, Valbonne-Sophia Antipolis, France.

[*]Corresponding author. Email: `emre.baspinar@cnrs.fr`

Abstract

We propose a new neural field model for migraine-related cortical spreading depression (CSD). The model follows the Wilson-Cowan-Amari [1, 2] formalism. It is based on an excitatory-inhibitory neuron population pair which is coupled to a potassium concentration variable. This model is spatially extended to a cortical layer. Therefore, it can model both the ignition and propagation of CSD. It controls the propagation speed via connection weights and contribution weight of each population activity to the potassium accumulation in the extracellular matrix. The simulation results regarding the propagation speed are in coherence with the experiment results given in [3].

1 Introduction

Cortical spreading depression (CSD) is a wave of neuronal depolarization that slowly spreads across the cortex. It is accompanied by a disturbance in ion concentration homeostasis, followed by a prolonged neuronal silence that may last for several minutes. This prolonged neuronal silence gives to the phenomenon its name, *depression*.

Similarities between the CSD propagation and the spread of migraine with visual aura lead to the hypothesis that CSD is the mechanism that evokes migraine aura [4]. In a recent report, electrophysiological recordings clearly demonstrated that spreading depolarization-induced spreading depression of spontaneous cortical activity was associated with symptomatic migraine aura in a patient [5]. Moreover, clinical studies have shown that CSD is closely associated with ischemic stroke and traumatic brain injury [6–8]. Therefore, it is important to better understand this phenomenon to develop preventive methods.

Nav1.1 is a voltage-gated sodium channel that plays a crucial role in the excitation of GABAergic type inhibitory neurons. SCN1A is the gene encoding for the Nav1.1 channel. It is the target of many mutations associated with either sporadic/familial hemiplegic migraine (FHM) [9–11], with severe consequences such as weakness of one side of the body, or epileptic disorders [12, 13].

Of the three responsible gene mutations that cause FHM, SCN1A mutations are known to be the ones that cause FHM type 3 (FHM3). Recently, SCN1A mutations leading to gain of function of the Nav1.1 channel were shown to be closely related to the occurrence of FHM3 [11, 13–16]. The gain of function implies hyperexcitability of interneurons. Counter-intuitively, it has been hypothesized that very high firing rate of interneurons can trigger CSD [6, 17, 18]. Recently, this has been shown to be one of the pathological mechanisms involved in migraine with aura [5], the category of FHM3, as well as in several other brain pathologies such as ischemic stroke and traumatic brain injury [6,17,18]. More specifically, it was shown, both *in vitro* and in a mouse model, that SCN1A mutations leading to Nav1.1 gain of function favor CSD initiation [11–16, 19–23]. Nevertheless, it is still not clear how the SNC1A mutation leading to the gain of function of Nav1.1 elicits the activity of GABAergic neurons and how this consequently induces the network hyperexcitability that generates CSD.

Despite its dramatic consequences, CSD has only recently been detected in humans [24, 25], and it remains difficult to detect it noninvasively in humans [26]. Its increasing clinical importance in brain disorders creates an urgent need for mathematical models that can account for the biological mechanisms at different levels. Following this line of research, we propose a mathematical model to contribute to a better understanding of this phenomenon, especially in the context of migraine at the neuronal population level. The novelty of the model

is that it takes into account the ionic modulation of the neuronal transfer functions. Moreover, unlike previous models, it reproduces not only ignition dynamics but also the propagation dynamics of CSD. The code package of the model implementation and simulations can be found in GitHub [27].

In Section 2 we present the hypothesis that motivates our model, as well as previous frameworks that have inspired the model. In Section 3 we present our model framework. In Section 5, we present our simulation results of CSD ignition and propagation. Finally, in Section 6, we conclude by summarizing the novelties and future perspectives.

2 Background

Three mechanisms have been hypothesized for the CSD ignition that follows hyperexcitability of inhibitory neurons in the case of FHM3 [14, 19, 20, 22, 28]: (i) the extracellular accumulation of potassium resulting from the potassium currents due to spiking of the inhibitory neurons. This can be observed during the time when the inhibitory neurons are firing at a high frequency. (ii) The KCC2 co-transporter increases extracellular potassium following intense inhibitory activity of interneurons. This situation may occur when intense GABA-ergic transmission occurs. In such cases, KCC2 attempts to transport potassium and chloride together to keep the intracellular chloride concentration in the excitatory cells low. This leads to potassium efflux, and consequently extracellular potassium accumulation increases [29–31]. (iii) The excitatory effects resulting from GABA-ergic transmission. Such effects could occur when KCC2 and possibly other homeostatic mechanisms reach their limits. At this point, the chloride gradient begins to weaken, and this situation could lead to depolarizing excitatory actions that follow the GABA-A receptor increasing its activity [32]. All of these mechanisms may induce, possibly in parallel, pyramidal cell excitability and trigger CSD.

Our hypothesis is that intense firing of interneurons may trigger the depolarization block which evokes CSD and leads to FHM3-type migraine. This hypothesis was investigated in [28], where a conductance-based model based on a pair of excitatory and inhibitory Hodgkin-Huxley cells was used. The coupling was based on a GABA-ergic synapse from the inhibitory to the excitatory cell and on a glutamatergic synapse from the excitatory to the inhibitory cell. An excitatory self-coupling was used to account for the effects of glutamatergic input on the excitatory cell. In addition, ion concentrations of the excitatory cell were dynamic, resulting in reversal potentials that varied slowly. The assumption of constant reversal potentials does not hold, as this assumption is rather for the cases where homeostatic equilibrium is maintained. In CSD, however, homeostatic equilibrium is violated, justifying the presence of slowly varying reversal potentials. This model was extended from [33], in which a Hodgkin-Huxley type neuron model was used to study the dynamics associated with epileptic activity, CSD, and spike generation, but without considering the role played by the hyperexcitation of interneurons. A similar model was used in [34] to investigate the effects of cell volume on dynamics related to epileptic activity and spreading depression. In a recent work [35], the model presented in [28] was extended to a framework in which, in addition to the relationship between SCN1A mutations leading to Nav1.1 gain of function and CSD initiation, the relationship between SCN1A mutations leading to Nav1.1 loss of function and epileptic activity was considered. Previous models for FHM3 or spreading depression did not consider Nav1.1 mutations on GABAergic neurons, and this is one of the contributions of our model framework as well as the models presented in [28, 35].

We use a Wilson-Cowan-Amari [1, 2] type neural field model. Neural populations are coupled to potassium concentration such that neural activity modulation via potassium accumulation in the extracellular matrix is considered. We model potassium concentration in a generic manner that accounts for all three aforementioned mechanisms (i), (ii) and (iii) associated with CSD ignition, which is identified as a depolarization block. The model is spatially extended to a cortical layer, therefore it can model both ignition and propagation of CSD.

3 Model framework

We interpret the spreading depression as propagating waves described by a rapidly evolving firing rate v and a slowly evolving extracellular potassium concentration k, and model it in terms of a neural field. A connectivity kernel captures the neural connectivity in the neural field. The field is coupled with a reaction-diffusion equation describing potassium diffusion.

Our neural field model is written as follows:

$$\begin{aligned}\frac{\partial v}{\partial t} &= -v + \int_Q w(x-y) s_p(v(y,t), k(y,t))\, dy + g_v(v,k) \\ \frac{\partial k}{\partial t} &= \delta \frac{\partial^2 k}{\partial x^2} + g_k(s, s_p(v,k), a, b) + I.\end{aligned} \tag{1}$$

Here v and k denote the firing rate and potassium concentration, respectively. They are inputs to the firing rate transfer function s_p, whose parameters are denoted by the vector p. We denote by $Q \in \mathbb{R}^2$ the cortical layer

where the CSD starts and propagates. We express the connectivity kernel as $w(x,y) = \frac{1}{2}\,\mathrm{e}^{-(x-y)^2}$. Here, g_v is a generic function representing the effect of potassium on the firing rate, and it denotes any potassium-related activity that affects the firing rate. Similarly, the effect of firing rate on potassium concentration is introduced by the function g_k, with parameters $a, b \geq 0$ and with s representing a specific sample of s_p, as will be explained in Section 3.2. We denote the external input by I, which is a localized potassium *puff*. The constant $\delta > 0$ ensures the unit coherency between the diffusion and the drift in the potassium concentration equation.

We assume that the CSD ignition and propagation are radially symmetric. Consequently, the propagation is radial and its velocity is constant; see Figure 4.

3.1 Firing rate transfer function

Recall that in a classical neural field, low inhibitory activity gives rise to high excitatory activity and high inhibitory activity gives rise to low excitatory activity. In our framework, the transfer function s_p takes into account the generalized excitatory activity that distinguishes very high inhibitory activity from high inhibitory activity. It is defined as

$$s_p(v,k) \coloneqq \begin{cases} \frac{1}{2(1+\mathrm{e}^{-\beta(v-h)})}, & k < k_1^* \\ \frac{1}{1+\mathrm{e}^{-\beta(v-h)}}, & k_1^* \leq k \leq k_2^* \\ 0, & k_2^* < k, \end{cases} \tag{2}$$

where $p = (\beta, v^*, k_1^*, k_2^*) \in \mathbb{R}^4$ denote the parameters. Here k_1^*, $k_2^* > 0$ denote the potassium thresholds, β represents the sharpness of the nonlinearity of s_p, and $h \in \mathbb{R}$ expresses the value of the half response voltage. The corresponding output of the transfer function to a very high inhibitory activity is a low excitatory activity or a silent phase. This property of the transfer function is due to a threshold effect. Unlike the classical neural field setup, where the transfer function depends only on the neural activity, in our framework the transfer function also depends on the time-dependent potassium concentration k; see Figure 1. Consequently, the same neural activity can produce different transfer function outputs depending on the potassium concentration. In other words, we observe a threshold effect when the potassium concentration is very high, i.e., when $k > k_2^*$. The transfer function has the typical nonlinear sigmoidal behavior for $k < k_1^*$ and $k_1^* < k < k_2^*$, where the maximum value of the transfer function is higher for the latter. The former corresponds to a low potassium concentration and thus a low inhibitory activity regime with $1/2$ as the maximum firing rate. The latter corresponds to a high potassium concentration and thus a high inhibitory activity with 1 as the maximum firing rate. A neural regime above the threshold with $k \geq k_2^*$ corresponds to a very high inhibitory activity, in which the potassium concentration is too high. This results in a low excitatory firing rate for all voltage activity v values and generates the depolarization block that marks the onset of CSD and triggers it; see Figure 2.

The system given by (1) models only the activity of the excitatory population. The inhibitory population activity is not explicitly included. The potassium related inhibitory activity is represented in terms of the potassium concentration variable k. In accordance with our hypothesis, the increase and decrease in potassium concentration reflects the increase and decrease in inhibitory population activity, respectively.

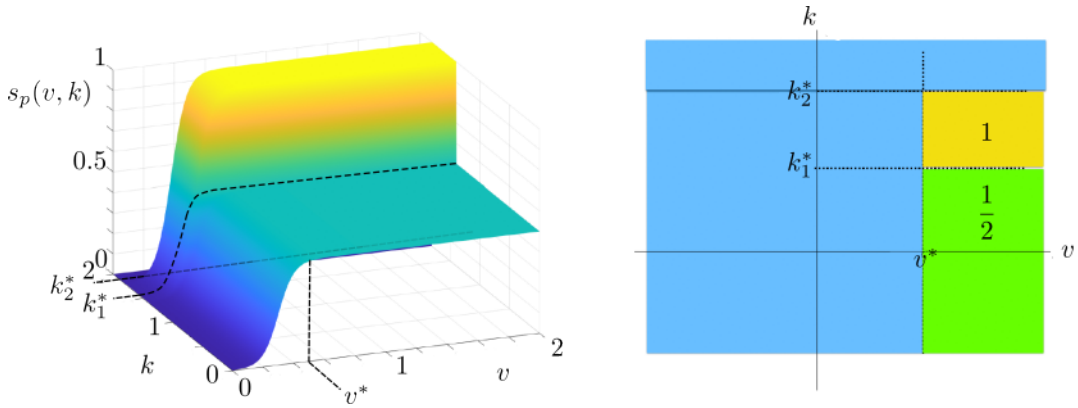

Figure 1: Left: Transfer function s_p with respect to the firing activity v and potassium concentration k. Right: Top view of the maximum and minimum values of the transfer function. The nonlinear regions are ignored.

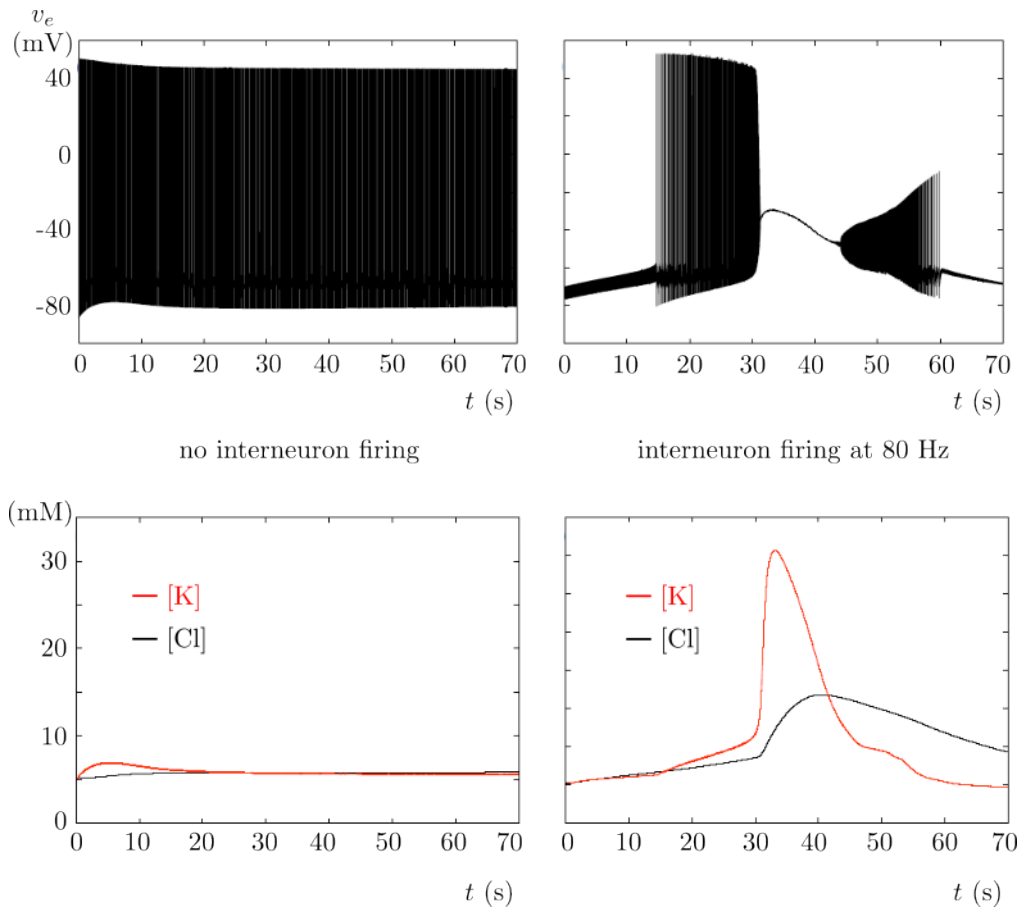

Figure 2: Some example CSD results of the Hodgkin-Huxley model framework presented in [28]. Time course of the excitatory cell membrane potential on the top and the corresponding extracellular ion concentration on the bottom. Top left: Tonic spiking excitatory cell without any coupling to the inhibitory cell. Bottom left: Corresponding extracellular potassium and chloride concentrations. Top right: Depolarization block of the excitatory cell with CSD following the block. Bottom right: Corresponding ion concentrations.

3.2 Potassium to firing rate transfer function

We consider all potassium-related effects on the firing rate of the excitatory population via g_v, a nonlinear function given by

$$g_v(v, k;\, \beta_v, k_v^*) \coloneqq \frac{1}{1 + \mathrm{e}^{-\beta_v (k - k_v^*)}}. \tag{3}$$

Here $\beta_v > 0$ and k_v^* denote the sharpness and k threshold, respectively. This is a generic function that models all potassium-related excitatory activity, with the exception of excitatory potassium build up due to potassium currents resulting from interneuron spikes. This latter type of activity is explicitly supplied to the system via the firing rate transfer function s_p. See Figure 3 for a simplified plot of g_v.

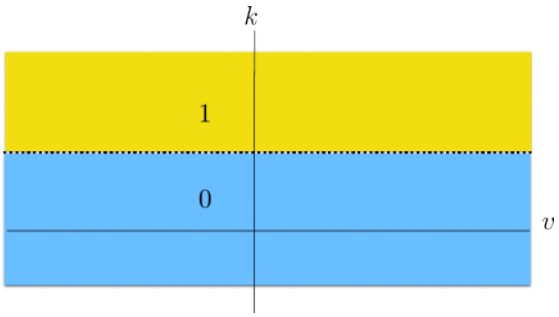

Figure 3: Potassium to rate transfer function g_v with respect to the excitatory firing rate v and potassium concentration k. Regions of the maximum and minimum values are represented by the yellow and blue colors, respectively.

3.3 Firing rate to potassium transfer function

We represent the effects of the interactions between the excitatory activity (or the inhibitory activity) and the potassium concentration on the potassium concentration with the nonlinear function g_k. We define g_k as follows:

$$g_k(s, s_p, a, b) \coloneqq \cosh(a(s - b\, s_p)), \tag{4}$$

with parameters $a, b \geq 0$, $s = s_p(v^*, k_1^*)$ and $s_p = s_p(v, k)$.

4 Extended model framework

We extend the model framework by explicitly representing the excitatory and inhibitory population firing rates, v_e and v_i, respectively. We define

$$\begin{aligned} Se(v_e, k, p) &\coloneqq \int_Q w_e(x - y) \xi_p(v_e(y, t), k(y, t))\, dy, \\ Si(v_i, k, q) &\coloneqq \int_Q w_i(x - y) \eta_q(v_i(y, t), k(y, t))\, dy, \end{aligned} \tag{5}$$

and then write the extended model equations as follows:

$$\begin{aligned} \tau \frac{\partial v_e}{\partial t} &= -v_e + c_{ee} Se(v_e, k, p) + c_{ei} Si(v_i, k, q) + g_v(v_e, k;\, \beta_e, k_{\nu_e}^* = k_v^*) \\ \tau \frac{\partial v_i}{\partial t} &= -v_i + c_{ie} Se(v_e, k, p) + c_{ii} Si(v_i, k, q) + g_v(v_i, k;\, \beta_i, k_{\nu_i}^* = k_v^*) \\ \tau \frac{\partial k}{\partial t} &= \delta \frac{\partial^2 k}{\partial x^2} + c_1\, g_k(\xi, \xi_p(v_e, k), a, b) + c_2\, g_k(\eta, \eta_p(v_i, k), a, b) + I. \end{aligned} \tag{6}$$

Here w_e and w_i denote the connectivity kernels corresponding to the excitatory and inhibitory populations, respectively. Similar to the previous model, but now separated for each population, g_v functions, possibly with different parameter sets, denote all potassium related activities interacting with the excitatory and inhibitory populations. Coefficients $0 < c_2 \leq c_1 < \infty$ weight the contributions of excitatory and inhibitory populations to extracellular potassium accumulation. Moreover, we choose $0 < \beta_i < \beta_e < \infty$ due to our hypothesis of that the excitatory activity associated with CSD results from the extracellular potassium accumulation. In other words, potassium concentration triggers firing of excitatory populations more readily than that of inhibitory populations with respect to the CSD ignition. Time scale $\tau > 0$ introduces a physical dimension to time. This

will be important in calculating the wave propagation velocity of a depolarization block. Finally, the transfer functions are denoted by ξ_p and η_q, where p and q are the parameters of the transfer functions. Here ξ and η are specific samples of ξ_p and η_q similarly to s appearing in (4). We define the transfer functions as

$$\xi_p(v_e, v_i, k) := s_p(v_e, k), \qquad \eta_q(v_i, k) := s_q(v_i, k), \tag{7}$$

where $-1 \leq c_{ei}, c_{ii} \leq 0$ and $0 \leq c_{ee}, c_{ie} \leq 1$ denote the cross and recurrent connectivity weights. The rest of the parameters is as in the previous model framework (1).

Our extended framework differs from previous framework given in (1) in three respects. First, the interaction of the inhibitory population with both the excitatory population and the potassium concentration is now explicit. Second, both excitatory and inhibitory connections are considered. Third, the cross population connections weights c_{ie}, c_{ei} are weaker in comparison to the recurrent connection weights c_{ee} and c_{ii} because we account for the connectivity differences related to the spatial distances between neurons.

5 CSD ignition and propagation

CSD ignition is a local phenomenon that begins in a small area of the cortical surface and then spreads over the entire cortical surface. In previous modeling frameworks, CSD initiation was studied [3, 28, 35], however, the propagation across the cortical surface was ignored. We show that our model framework successfully reproduces both the initiation and propagation of the phenomenon.

We assume that the cortical surface is a disk and that the propagation of the CSD is radial, as in the previous framework given by (1). In other words, we restrict neuronal connectivity to radiality. We measure the propagation velocity along the radial axes by assuming that the angular component of the propagation velocity is zero. Therefore, we can define the cortical disk as a set of partitions Q_k of lines running from the center of the disk, where the CSD source is located, toward the cortical edge such that

$$Q = \bigcup_{k=1,2,\ldots,\infty} Q_k. \tag{8}$$

This simplifies the problem and allows the study of CSD ignition and propagation on a single partition Q_k.

We denote the horizontal partition as Q_1 and assume that the neuronal population pairs lying along Q_1 have equidistant spacing $h_x = \frac{2L_x}{N-1}$, where the length of Q_1 is $2L_x = 400$ mm and N is the total number of population pairs in each partition Q_k.

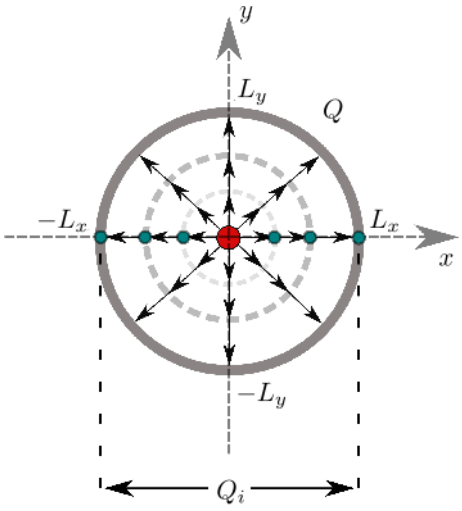

Figure 4: Illustration of the propagation of a radial depolarization block on cortical disk Q. Ignition occurs at the source point marked in red. The boundary of the disk is shown by the bold outermost circle with radius $L_x = L_y$. The arrows represent the directions of propagation. Dashed circles illustrate the sets of two different propagating v_e values. Neurons represented by green dots lie on the horizontal partition Q_1.

Figure 5 shows the space-time diagram of an example of depolarization block wave which emerges from the population pair located at the center of the cortical disk. This wave propagates radially and symmetrically with a constant velocity towards the cortical disk boundary. An external input in the form of a potassium puff evokes the propagation of the depolarization block wave. The increasing potassium concentration gives rise to increasing excitatory activity, thus to depolarization block propagating towards the peripheral populations. See

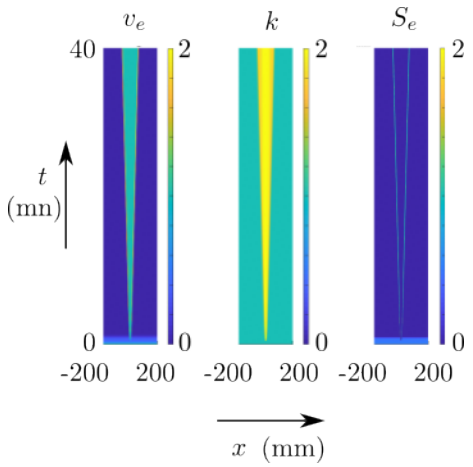

Figure 5: Diagrams of the propagation of excitatory population potential, the expansion of potassium concentration and the propagation of the excitatory population firing rate in time and space.

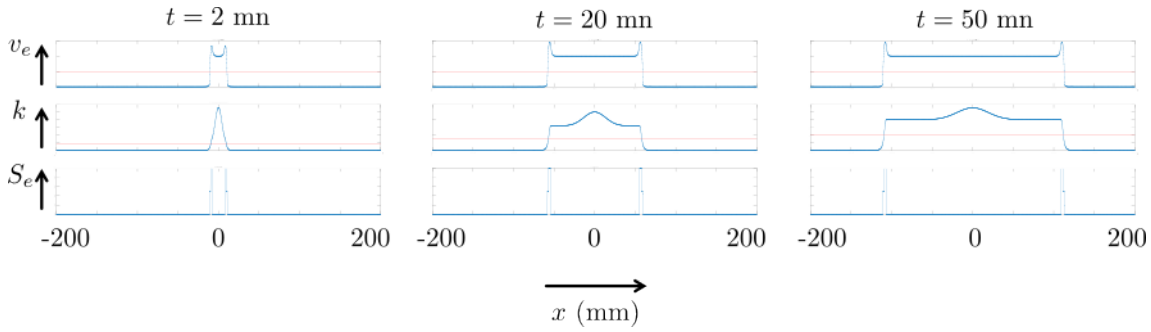

Figure 6: Plots of excitatory population potential and firing rate propagating towards the edge of the cortical disk in the top and bottom rows, respectively; and the plots of the expanding potassium concentration towards the cortical disk boundary in the middle row. The columns correspond to $t = 2$, 20 and 50 mn from left to right. Red horizontal lines show v_e^* and k_v^* in v_e adn k plots, respectively.

Figure 6, in which we provide the plots of a propagating excitatory population potential and firing rate, as well as the expanding potassium concentration over the populations.

In Figure 7, we see the propagation of the excitatory and inhibitory population activities at $t = 200$ mn on the left and right panels, respectively. We consider the peak and the highest point of the plateau edges as the position of the propagating waves at the given instant. We observe that the excitatory activity wave is followed by an inhibitory wave. This models the suppression of the brain activity, i.e., the depression, which follows the slowly propagating wave of depolarization as observed in the migraine cases with CSD [36].

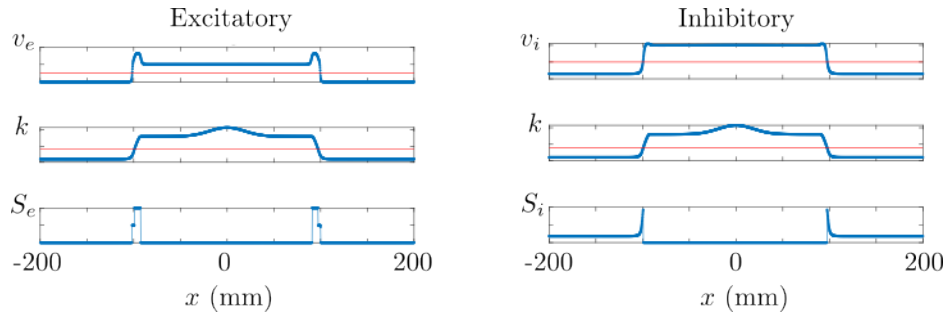

Figure 7: Plots of the average membrane potentials of both excitatory and inhibitory populations (top) together with the transfer functions outputs (bottom) and the extracellular potassium (middle). The plots are obtained at $t = 200$ mn. Red horizontal lines show v_e^* (or v_i^*) and k_v^* in v_e (or v_i) and k plots, respectively.

5.1 Emergence of propagating depolarization waves

In accordance with our hypothesis, the model generates propagating depolarization waves due to the high potassium density in the extracellular matrix, caused by the high inhibitory activity. The depolarization waves emerge once we turn on the potassium variable k, as well as the interactions between the excitatory and inhibitory population average membrane potentials v_e and v_i as shown in Figure 8. We observe that the depolarization block propagation, therefore the CSD ignition, starts as soon as we turn on $c = c_1 = c_2$. The propagation velocity and life span of the propagating wave depends on both c and k_v^* as seen in Figures 9 and 10.

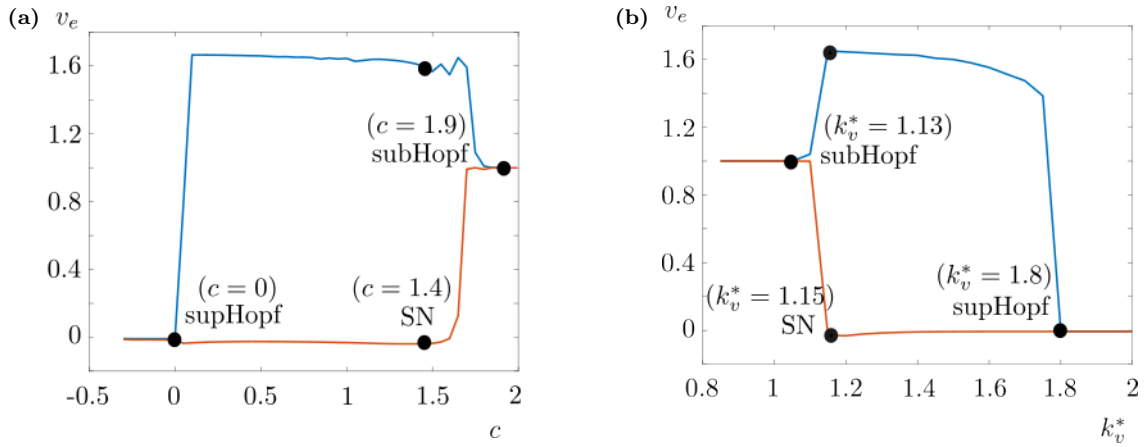

Figure 8: Bifurcation diagrams with respect to the bifurcation parameters c and k_v^* in (a) and (b), respectively. Here supHopf and subHopf denote sub- and sup-critical Hopf bifurcations, respectively. SN represents a saddle node bifurcation. The connectivity weights are fixed in both diagrams as $c_{ie} = -c_{ei} = 0.25$, $c_{ee} = 1$ and $c_{ii} = -1$.

In Figure 9a, we observe that for the c values around 0, there is an ignition of a wave but it converges to a stationary solution, which corresponds to a locally fixed non-zero voltage (v_e) value and to 0 elsewhere. As we increase c, a propagating wave emerges. This corresponds to the region between the supHopf and SN, therefore stable limit cycles, as shown in Figure 8a. As we increase c further, we observe in Figure 9b that stable limit cycles transform into unstable limit cycles as the system undergoes the SN. This results in that the propagating wave disappears, and a transient propagating wave occurs. Finally, as the system goes through the subHopf with increasing c beyond 1.9, the transient wave disappears and the system converges to a fixed point, resulting in no wave activity.

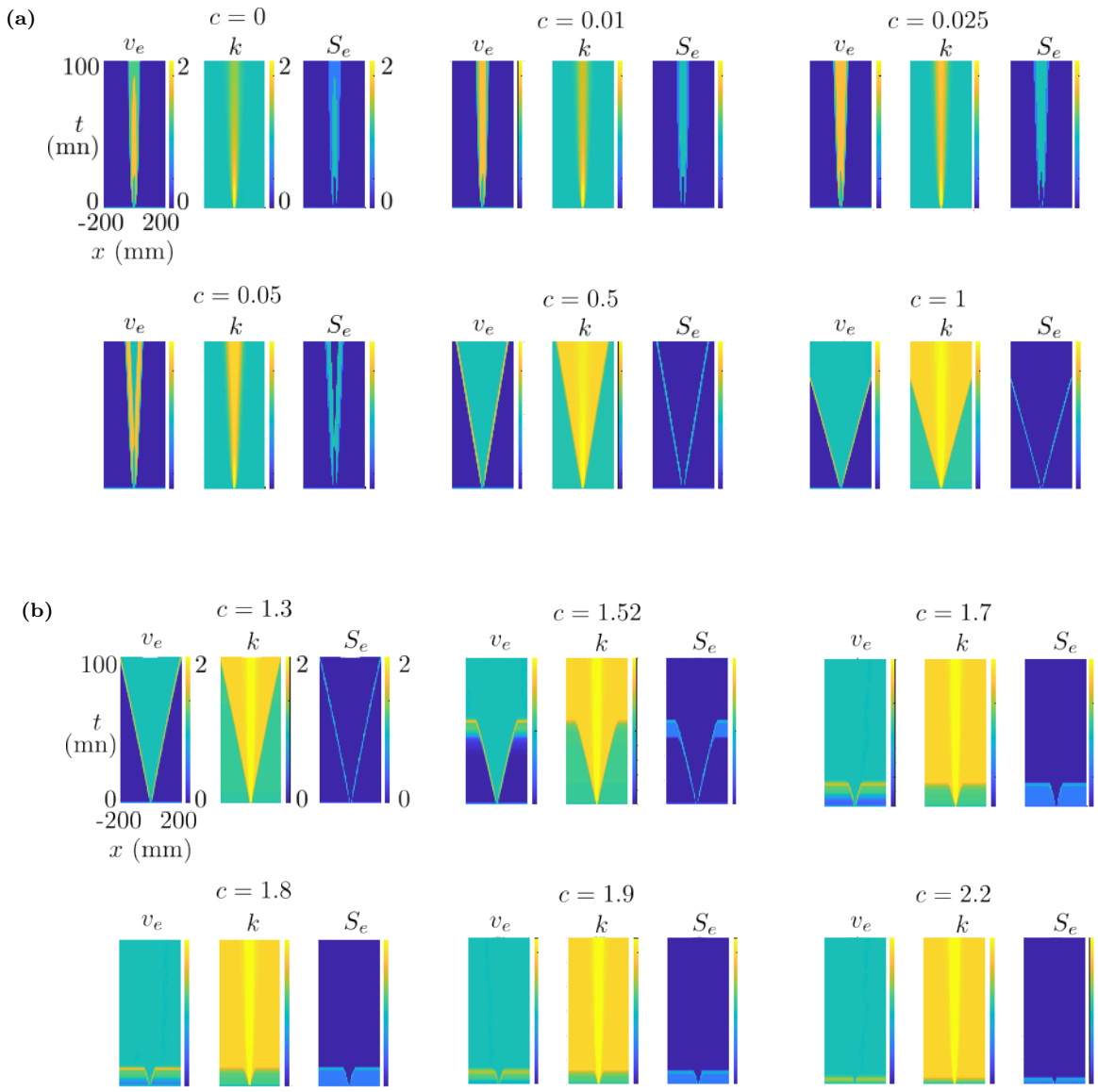

Figure 9: Space-time diagrams of neural activity with increasing $c = c_1 = c_2$ values around the supHopf and subHopf shown in Figure 8a. Here $k_v^* = 1.2$. Axes and legend values are given in the top left plots of each panel, and they are the same for the rest of the plots in their corresponding panels. **(a)** There is no propagating wave when there is no potassium contribution ($c = 0$) from the populations. System (6) is in a steady-state and no propagation occurs. As we turn on c, a propagating depolarization block emerges and it propagates faster as we increase c. **(b)** The propagating depolarization waves become transient after the SN ($1.9 > c > 1.4$). They vanish completely after the subHopf ($c > 1.9$).

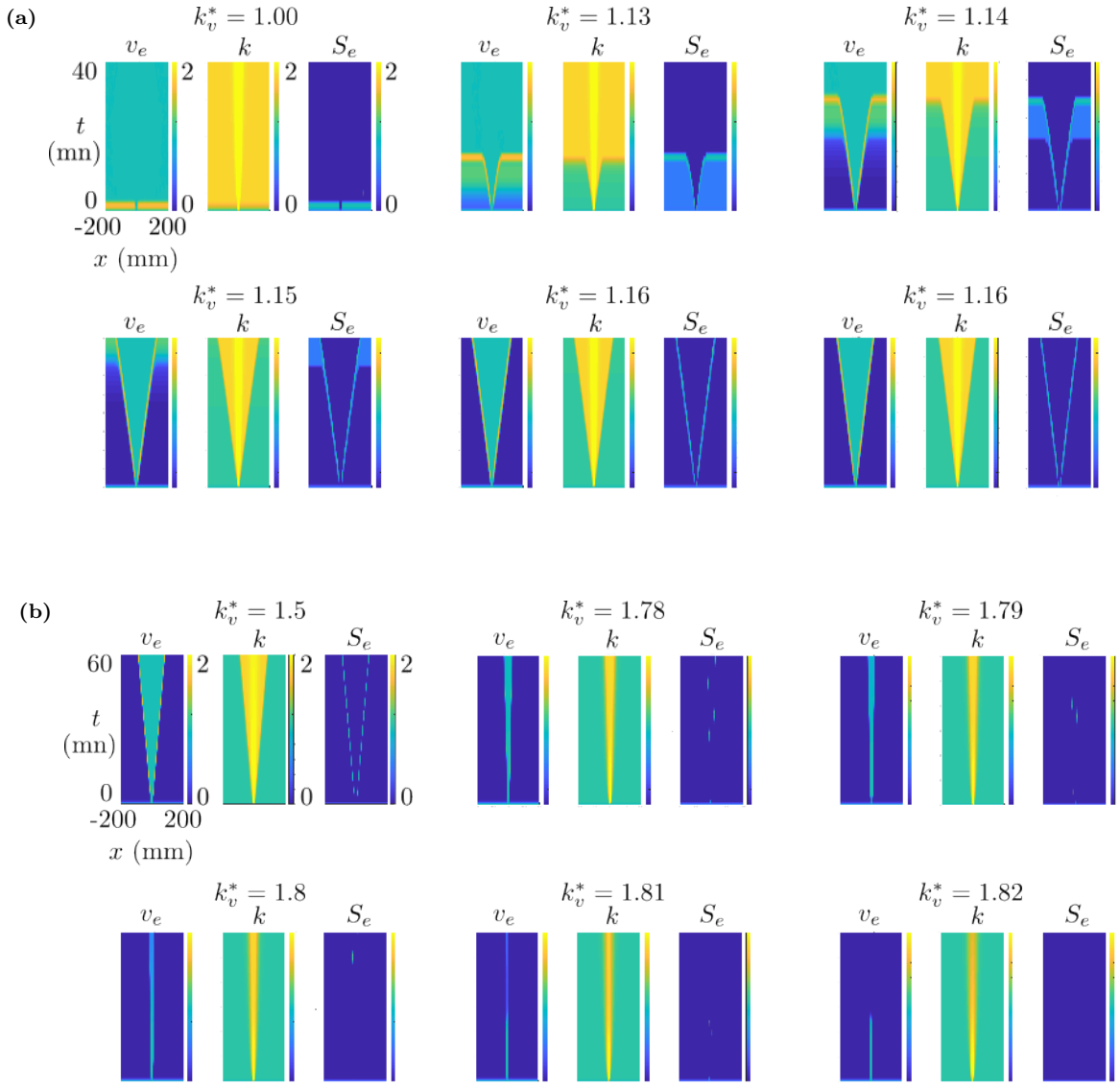

Figure 10: Space-time diagrams of the neural activity with increasing k_v^* values around the subHopf and supHopf shown in Figure 8b. Here $c = 1$. Axes and legend values are given in the top left plots of each panel, and they are the same for the rest of the plots in their corresponding panels. **(a)** We observe short transient waves before the subHopf ($k_v^* \leq 1.15$), or no wave as in the case with $k_v^* = 1.0$. As the system goes through the subHopf bifurcation ($k_v^* > 1.15$), stable limit cycles, i.e., propagating depolarization blocks, appear.**(b)** The propagating depolarization blocks disappear as the system goes through the supHopf and silent activity patterns appear, indicating no neural activity beyond supHopf ($k_v^* > 1.8$).

We observe in Figure 8b a symmetric diagram with respect to Figure 8a. In Figure 8b, stationary solutions vanish and unstable limit cycles emerge while the system goes through the supHopf as we increase k_v^*. There is no activity before the subHopf, see Figure 13a. As system goes through the subHopf, transient waves appear. As we increase k_v^* more, the system goes through the SN, after which the unstable limit cycles vanish and stable limit cycles appear as shown in Figure 13a. Those stable limit cycles correspond to propagating deplorization blocks spreading across the whole brain. Finally, the system goes through the supHopf as we increase k_v^* further and the limit cycles vanish. The system converges to a fixed point for each $k_v^* > 1.8$ beyond the supHopf, resulting in a short transient period and no activity afterward; see Figure 10.

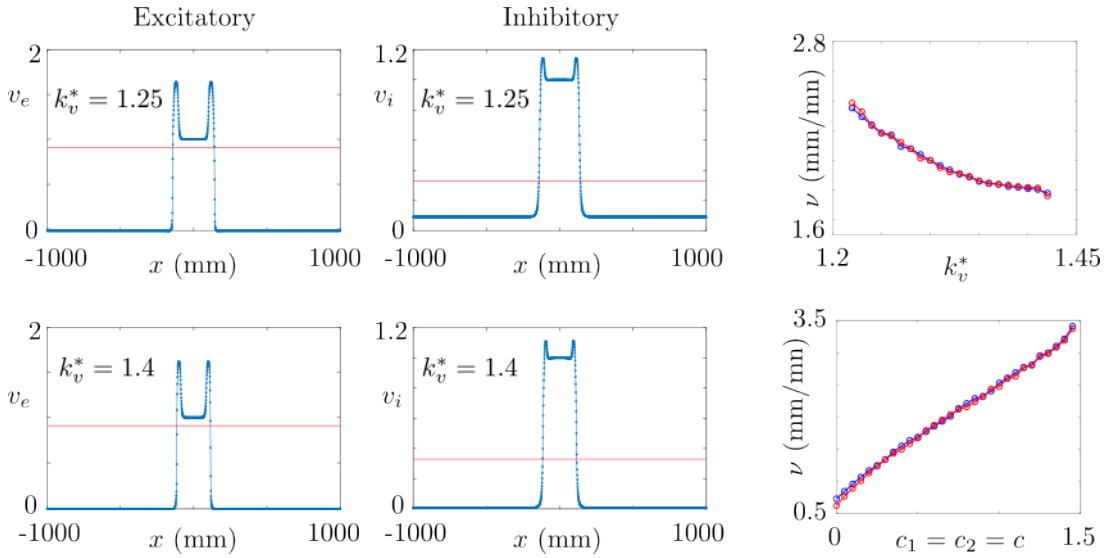

Figure 11: Left: Propagating excitatory population membrane potential for two different k_v^* values. Horizontal red line shows the threshold value to detecting the wave front. Right top: Plot of the propagation velocity of depolarization block with respect to increasing k_v^* values, with $c_1 = c_2 = c = 1$. Right bottom: The same but with respect to increasing c values, where $k_v^* = 1.2$.

5.2 Potassium production and propagation velocity

Propagation velocity of the depolarization block can be controlled via the potassium concentration threshold parameters $k_{\nu_e}^*$ and $k_{\nu_i}^*$. We provide the plots of propagating excitatory potentials across the cortical disk with different $k_{\nu_e}^* = k_{\nu_i}^* = k_\nu^*$ parameters and at time instant $t = 50$ mn on the left panel of Figure 11, where we see that the propagation velocity decreases with increasing k_ν^*. We choose $k_{\nu_e} = k_{\nu_i}$, however, it is possible to choose them differently in the generic case. We provide the decreasing trend of the propagation velocity ν with respect to increasing $k_{\nu_e}^* = k_{\nu_i}^* = k_\nu^*$ on the right panel of Figure 11 for both excitatory (blue) and inhibitory (red) populations. We observe that the populations are synchronized, propagation velocity is the same for both population types. In accordance with the experimental observations [37, 38], the propagating depolarization wave leaves a period of hyperpolarization, a suppressed activity behind.

We show the effects of changing $c_1 = c_2 = c$ values on the propagation velocity for both excitatory (blue) and inhibitory (red) populations in the right bottom panel of Figure 11. Increasing c provides stronger contribution to the extracellular potassium accumulation. This results in increasing propagation velocity as expected.

The propagation velocity ν is measured based on

$$\nu = \frac{h_x(n_{\text{th}} - N/2)}{t_F}. \tag{9}$$

Here n_{th} and t_F denote the index of the population pair having equal potential to preset threshold and the time instant at which the measurement is made, that is the final time, respectively. Those results show that our model framework has full control over the propagation velocity of the depolarization block via the parameters $k_{\nu_e}^* = k_{\nu_i}^* = k_v^* = 1.1$, c_1 and c_2.

In certain cases, the contribution of the excitatory populations to potassium accumulation in the extracellular matrix can be stronger than the contribution of the inhibitory populations, i.e., $c_1 > c_2$. This is due to the fact that there are more excitatory cells than inhibitory cells in the cortex; and the excitatory cells are usually bigger in size. Therefore, their total activity is higher compared to the inhibitory cells. They can produce more potassium accumulation. Such behavior with $c_1 > c_2$ can be reproduced by our model; see Figure 12.

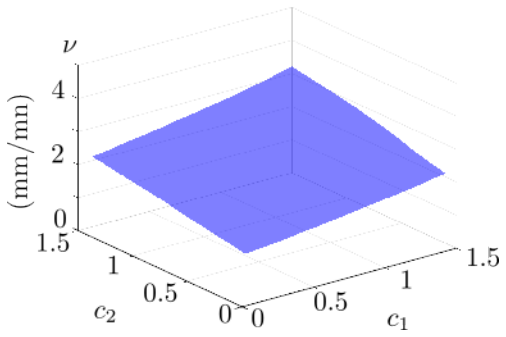

Figure 12: Propagation speed with respect to c_1 and c_2.

5.3 Connectivity and propagation velocity

We provide the results related to connectivity weights and their effects on propagation velocity of depolarization block. We model block of Glutamatergic receptors (suppression of excitation) by fixing $c_{ee}, c_{ie} = 0$ and block of GABA-A receptors (suppression of inhibition) by fixing $c_{ii}, c_{ei} = 0$. We observe in Figure 13 that, as we remove the block of Glutamatergic receptors by increasing c_{ee}, c_{ie}, the depolarization block propagates faster; and as we remove the block of GABA-A receptor by increasing c_{ii}, c_{ei}, the depolarization block propagates rather slowly. Those results overlap with the experiment results presented in [3, Figure 7F]. Moreover, the range of ν for the simulated c_1 and c_2 values span the experimentally observed propagation velocity of CSD, which is 2-4 mm/mn approximately [39], and it can be adjusted by changing the time scale parameter τ in (6).

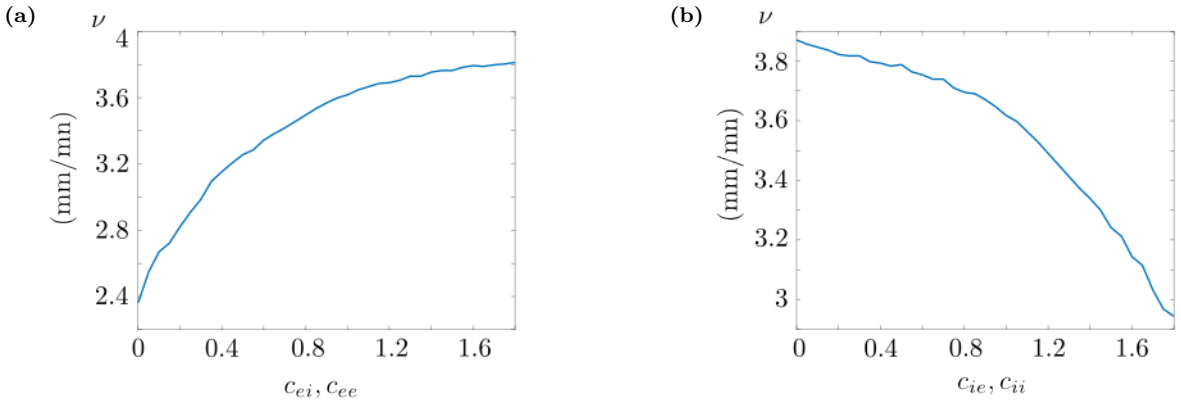

Figure 13: Propagation velocity with respect to connection weights. Small c_{ee}, c_{ie} model the blocking of Glutamatergic receptors and small c_{ii}, c_{ei} model the blocking of GABA-A receptors. **(a)** Propagation velocity increases with stronger excitatory connections. Here $c_{ii}, c_{ei} = -1$. **(b)** It decreases with stronger inhibitory connections. Here $c_{ee}, c_{ie} = 1$.

6 Discussion

We presented a novel neural field model for CSD. The model is based on a Wilson-Cowan-Amari type framework in which an excitatory-inhibitory neuron population pair is coupled to potassium concentration. The potassium concentration is described in terms of a reaction-diffusion equation.

The model has several novelties. First, in the firing rate transfer function, we include not only the firing activity as in the classical Wilson-Cowan model, but also the extracellular potassium concentration. The potassium concentration is dynamic and it depends on the firing activity. In addition, a transfer function from potassium to firing rate is introduced as an input to firing activity. This interaction between the firing activity and potassium concentration characterizes the interneuron activity that unexpectedly leads to the triggering of CSD in the same line as our hypothesis. Second, in contrast to the models presented in [28, 35], our model can represent not only the CSD ignition but also the CSD propagation, which starts locally with ignition and spreads globally across the cortical layer. Third, the propagation velocity can be easily adjusted. In this way, we can study the layer-specific features of CSD, especially its propagation velocity, which is higher in the upper layers of the neocortex than in the lower layers [40–42]. Fourth, time scale τ appearing in (6) can be tuned according to the

participant the experiments such that the system captures the overlap between the simulated and experimentally observed propagation velocities. This provides a strong flexibility to our model in the sense that it can be tuned to each participant in the experiment by varying τ so that a full overlap in propagation velocity can be provided for the subject. Finally, this model can provide the effects of changes in connection and potassium contribution weights of different populations. These parameters cannot be controlled in the experiment setups.

The first perspective regarding our model is its extension to epileptic CSD. Mutations of SCN1A may result in also loss of function of Nav1.1 [12,13,16,43,44] and this might lead to the reduced excitability of the inhibitory neurons [45]. Such mutations are closely related to epileptic disorders, in particular to Dravet syndrome [46,47], which is a severe type of epileptic pathologies that are resistant to antiepileptic medications. The case of Dravet syndrome is less counter-intuitive compared to what is observed in FHM3 case considered here, because reduced inhibition naturally results in hyperexcitability of excitatory neurons and this evokes CSD. Our model can be adapted in a straightforward way to such epileptic cases of CSD.

The second perspective is that our model can be extended also to astrocytes, which constitute an active research area in migraine and epilepsy [48–50]. These are the brain cells which modulate neural interactions. They can be inserted in our model equations (6) as a third cell population coupled to the excitatory and inhibitory populations. It will correspond to a slow time scale since astrocyte activity is measured in terms of ionic activity, which changes more slowly in time compared to the electrical activity measured from neurons.

Appendix

Parameters used in Figures 8-13 are as follows:

$$\begin{aligned} &\delta = 1, \quad h = h_e = h_i = 0.3, \quad \beta_e = \beta_{v_e} = 100, \quad \beta_i = \beta_{v_i} = 10, v_e^* = v_i^* = 0.5, \\ &k_v^* = 1.2, \quad c_1 = c_2 = c = 1, \quad c_{ei} = -0.25, \quad c_{ie} = 0.25, \quad c_{ee} = 1, \quad c_{ii} = -1. \end{aligned} \tag{10}$$

We choose $k_1^* = 1.4$, $k_2^* = 1.8$ for excitatory populations and $k_1^* = 1.0$, $k_2^* = 1.4$ for inhibitory populations.

References

[1] Hugh R Wilson and Jack D Cowan. Excitatory and inhibitory interactions in localized populations of model neurons. *Biophysical journal*, 12(1):1–24, 1972.

[2] Shun-ichi Amari. Dynamics of pattern formation in lateral-inhibition type neural fields. *Biological cybernetics*, 27(2):77–87, 1977.

[3] Oana Chever, Sarah Zerimech, Paolo Scalmani, Louisiane Lemaire, Lara Pizzamiglio, Alexandre Loucif, Marion Ayrault, Martin Krupa, Mathieu Desroches, Fabrice Duprat, et al. Initiation of migraine-related cortical spreading depolarization by hyperactivity of GABAergic neurons and Na_V 1.1 channels. *The Journal of Clinical Investigation*, 131(21), 2021.

[4] AAP Leo and RS Morison. Propagation of spreading cortical depression. *Journal of Neurophysiology*, 8(1):33–45, 1945.

[5] Sebastian Major, Shufan Huo, Coline L Lemale, Eberhard Siebert, Denny Milakara, Johannes Woitzik, Karen Gertz, and Jens P Dreier. Direct electrophysiological evidence that spreading depolarization-induced spreading depression is the pathophysiological correlate of the migraine aura and a review of the spreading depolarization continuum of acute neuronal mass injury. *GeroScience*, 42(1):57–80, 2020.

[6] Daniela Pietrobon and Michael A Moskowitz. Chaos and commotion in the wake of cortical spreading depression and spreading depolarizations. *Nature Reviews Neuroscience*, 15(6):379–393, 2014.

[7] Jens P Dreier and Clemens Reiffurth. The stroke-migraine depolarization continuum. *Neuron*, 86(4):902–922, 2015.

[8] Jed A Hartings, C William Shuttleworth, Sergei A Kirov, Cenk Ayata, Jason M Hinzman, Brandon Foreman, R David Andrew, Martyn G Boutelle, KC Brennan, Andrew P Carlson, et al. The continuum of spreading depolarizations in acute cortical lesion development: examining leao's legacy. *Journal of Cerebral Blood Flow & Metabolism*, 37(5):1571–1594, 2017.

[9] Martin Dichgans, Tobias Freilinger, Gertrud Eckstein, Elena Babini, Bettina Lorenz-Depiereux, Saskia Biskup, Michel D Ferrari, Jürgen Herzog, Arn MJM van den Maagdenberg, Michael Pusch, et al. Mutation in the neuronal voltage-gated sodium channel SCN1A in familial hemiplegic migraine. *The Lancet*, 366(9483):371–377, 2005.

[10] Na Shao, Haining Zhang, Xue Wang, Wuqiong Zhang, Miaomiao Yu, and Hongmei Meng. Familial hemiplegic migraine type 3 (FHM3) with an SCN1A mutation in a Chinese family: A case report. *Frontiers in Neurology*, 9:976, 2018.

[11] Sandra Dhifallah, Eric Lancaster, Shana Merrill, Nathalie Leroudier, Massimo Mantegazza, and Sandrine Cestèle. Gain of function for the SCN1A/hNav1.1-L1670W mutation responsible for familial hemiplegic migraine. *Frontiers in Molecular Neuroscience*, 11:232, 2018.

[12] H Yu Frank, Massimo Mantegazza, Ruth E Westenbroek, Carol A Robbins, Franck Kalume, Kimberly A Burton, William J Spain, G Stanley McKnight, Todd Scheuer, and William A Catterall. Reduced sodium current in GABAergic interneurons in a mouse model of severe myoclonic epilepsy in infancy. *Nature Neuroscience*, 9(9):1142–1149, 2006.

[13] Massimo Mantegazza and Vania Broccoli. SCN1A/NaV1.1 channelopathies: Mechanisms in expression systems, animal models, and human iPSC models. *Epilepsia*, 60:S25–S38, 2019.

[14] Sandrine Cestèle, Emanuele Schiavon, Raffaella Rusconi, Silvana Franceschetti, and Massimo Mantegazza. Nonfunctional NaV1.1 familial hemiplegic migraine mutant transformed into gain of function by partial rescue of folding defects. *Proceedings of the National Academy of Sciences*, 110(43):17546–17551, 2013.

[15] Sara Bertelli, Raffaella Barbieri, Michael Pusch, and Paola Gavazzo. Gain of function of sporadic/familial hemiplegic migraine-causing SCN1A mutations: Use of an optimized cDNA. *Cephalalgia*, 39(4):477–488, 2019.

[16] Massimo Mantegazza, Sandrine Cestèle, and William Catterall. Sodium channelopathies of skeletal muscle and brain. *Physiological Reviews*, 2021.

[17] Martin Lauritzen. Pathophysiology of the migraine aura: the spreading depression theory. *Brain*, 117(1):199–210, 1994.

[18] Michel D Ferrari, Roselin R Klever, Gisela M Terwindt, Cenk Ayata, and Arn MJM van den Maagdenberg. Migraine pathophysiology: lessons from mouse models and human genetics. *The Lancet Neurology*, 14(1):65–80, 2015.

[19] Sandrine Cestèle, Paolo Scalmani, Raffaella Rusconi, Benedetta Terragni, Silvana Franceschetti, and Massimo Mantegazza. Self-limited hyperexcitability: functional effect of a familial hemiplegic migraine mutation of the Nav1. 1 (SCN1A) Na+ channel. *Journal of Neuroscience*, 28(29):7273–7283, 2008.

[20] Sandrine Cestèle, Angelo Labate, Raffaella Rusconi, Patrizia Tarantino, Laura Mumoli, Silvana Franceschetti, Grazia Annesi, Massimo Mantegazza, and Antonio Gambardella. Divergent effects of the T1174S SCN1A mutation associated with seizures and hemiplegic migraine. *Epilepsia*, 54(5):927–935, 2013.

[21] Chunxiang Fan, Stefan Wolking, Frank Lehmann-Horn, Ulrike BS Hedrich, Tobias Freilinger, Holger Lerche, Guntram Borck, Christian Kubisch, and Karin Jurkat-Rott. Early-onset familial hemiplegic migraine due to a novel SCN1A mutation. *Cephalalgia*, 36(13):1238–1247, 2016.

[22] Massimo Mantegazza and Sandrine Cestèle. Pathophysiological mechanisms of migraine and epilepsy: similarities and differences. *Neuroscience Letters*, 667:92–102, 2018.

[23] Raffaella Barbieri, Sara Bertelli, Michael Pusch, and Paola Gavazzo. Late sodium current blocker GS967 inhibits persistent currents induced by familial hemiplegic migraine type 3 mutations of the SCN1A gene. *The Journal of Headache and Pain*, 20(1):1–13, 2019.

[24] Avraham Mayevsky, Avi Doron, Tamar Manor, Sigal Meilin, Nili Zarchin, and George E Ouaknine. Cortical spreading depression recorded from the human brain using a multiparametric monitoring system. *Brain Research*, 740(1-2):268–274, 1996.

[25] Martin Fabricius, Susanne Fuhr, Robin Bhatia, Martyn Boutelle, Parastoo Hashemi, Anthony J Strong, and Martin Lauritzen. Cortical spreading depression and peri-infarct depolarization in acutely injured human cerebral cortex. *Brain*, 129(3):778–790, 2006.

[26] Bas-Jan Zandt, Bennie ten Haken, Michel JAM van Putten, and Markus A Dahlem. How does spreading depression spread? physiology and modeling. *Reviews in the Neurosciences*, 26(2):183–198, 2015.

[27] Emre Baspinar and Daniele Avitabile. A neural field model for cortical spreading depression. *Matlab code package*, GitHub: https://github.com/emrebasp/A-neural-field-model-for-cortical-spreading-depression.git.

[28] Mathieu Desroches, Olivier Faugeras, Martin Krupa, and Massimo Mantegazza. Modeling cortical spreading depression induced by the hyperactivity of interneurons. *Journal of Computational Neuroscience*, 47(2):125–140, 2019.

[29] Tero Viitanen, Eva Ruusuvuori, Kai Kaila, and Juha Voipio. The K+-Cl cotransporter KCC2 promotes GABAergic excitation in the mature rat hippocampus. *The Journal of Physiology*, 588(9):1527–1540, 2010.

[30] Nicolas Doyon, Steven A Prescott, Annie Castonguay, Antoine G. Godin, Helmut Kröger, and Yves De Koninck. Efficacy of synaptic inhibition depends on multiple, dynamically interacting mechanisms implicated in chloride homeostasis. *PLoS Computational Biology*, 7(9):e1002149, 2011.

[31] Kai Kaila, Theodore J. Price, John A. Payne, Martin Puskarjov, and Juha Voipio. Cation-chloride cotransporters in neuronal development, plasticity and disease. *Nature Reviews Neuroscience*, 15(10):637–654, 2014.

[32] Kyle P. Lillis, Mark A. Kramer, Jerome Mertz, Kevin J Staley, and John A. White. Pyramidal cells accumulate chloride at seizure onset. *Neurobiology of Disease*, 47(3):358–366, 2012.

[33] Yina Wei, Ghanim Ullah, and Steven J Schiff. Unification of neuronal spikes, seizures, and spreading depression. *Journal of Neuroscience*, 34(35):11733–11743, 2014.

[34] Ghanim Ullah, Yina Wei, Markus A Dahlem, Martin Wechselberger, and Steven J Schiff. The role of cell volume in the dynamics of seizure, spreading depression, and anoxic depolarization. *PLoS Computational Biology*, 11(8):e1004414, 2015.

[35] Louisiane Lemaire, Mathieu Desroches, Martin Krupa, Lara Pizzamiglio, Paolo Scalmani, and Massimo Mantegazza. Modeling nav1. 1/scn1a sodium channel mutations in a microcircuit with realistic ion concentration dynamics suggests differential gabaergic mechanisms leading to hyperexcitability in epilepsy and hemiplegic migraine. *PLoS Computational Biology*, 17(7):e1009239, 2021.

[36] Andrew C Charles and Serapio M Baca. Cortical spreading depression and migraine. *Nature Reviews Neurology*, 9(11):637–644, 2013.

[37] I Garza, TJ Schwedt, CE Robertson, and JH Smith. Headache and other craniofacial pain. *Bradley's Neurology in Clinical Practice. 7th ed. Philadelphia, PA: Elsevier*, pages 1686–719, 2016.

[38] David Borsook, Nasim Maleki, and Rami Burstein. Chapter 42 - migraine. In Michael J. Zigmond, Lewis P. Rowland, and Joseph T. Coyle, editors, *Neurobiology of Brain Disorders*, pages 693–708. Academic Press, San Diego, 2015.

[39] Aristides AP Leao. Spreading depression of activity in the cerebral cortex. *Journal of Neurophysiology*, 7(6):359–390, 1944.

[40] Aristides AP Leo. Further observations on the spreading depression of activity in the cerebral cortex. *Journal of Neurophysiology*, 10(6):409–414, 1947.

[41] Trent A Basarsky, Steven N Duffy, R David Andrew, and Brian A MacVicar. Imaging spreading depression and associated intracellular calcium waves in brain slices. *Journal of Neuroscience*, 18(18):7189–7199, 1998.

[42] Sarah Zerimech, Oana Chever, Paolo Scalmani, Lara Pizzamiglio, Fabrice Duprat, and Massimo Mantegazza. Cholinergic modulation inhibits cortical spreading depression in mouse neocortex through activation of muscarinic receptors and decreased excitatory/inhibitory drive. *Neuropharmacology*, 166:107951, 2020.

[43] Ikuo Ogiwara, Hiroyuki Miyamoto, Noriyuki Morita, Nafiseh Atapour, Emi Mazaki, Ikuyo Inoue, Tamaki Takeuchi, Shigeyoshi Itohara, Yuchio Yanagawa, Kunihiko Obata, et al. Nav1. 1 localizes to axons of parvalbumin-positive inhibitory interneurons: a circuit basis for epileptic seizures in mice carrying an scn1a gene mutation. *Journal of Neuroscience*, 27(22):5903–5914, 2007.

[44] Ulrike BS Hedrich, Camille Liautard, Daniel Kirschenbaum, Martin Pofahl, Jennifer Lavigne, Yuanyuan Liu, Stephan Theiss, Johannes Slotta, Andrew Escayg, Marcel Dihné, et al. Impaired action potential initiation in gabaergic interneurons causes hyperexcitable networks in an epileptic mouse model carrying a human nav1. 1 mutation. *Journal of Neuroscience*, 34(45):14874–14889, 2014.

[45] Lieve Claes, Jurgen Del-Favero, Berten Ceulemans, Lieven Lagae, Christine Van Broeckhoven, and Peter De Jonghe. De novo mutations in the sodium-channel gene SCN1A cause severe myoclonic epilepsy of infancy. *The American Journal of Human Genetics*, 68(6):1327–1332, 2001.

[46] Ian O Miller and Marcio A Sotero de Menezes. *SCN1A Seizure Disorders*. University of Washington, Seattle, Seattle (WA), 1993.

[47] Takashi Sugawara, Yuji Tsurubuchi, Kishan Lal Agarwala, Masatoshi Ito, Goryu Fukuma, Emi Mazaki-Miyazaki, Hiroshi Nagafuji, Masaharu Noda, Keiji Imoto, Kazumaru Wada, et al. A missense mutation of the Na+ channel αII subunit gene Nav1.2 in a patient with febrile and afebrile seizures causes channel dysfunction. *Proceedings of the National Academy of Sciences*, 98(11):6384–6389, 2001.

[48] Michael A Rogawski. Common pathophysiologic mechanisms in migraine and epilepsy. *Archives of Neurology*, 65(6):709–714, 2008.

[49] Clizia Capuani, Marcello Melone, Angelita Tottene, Luca Bragina, Giovanna Crivellaro, Mirko Santello, Giorgio Casari, Fiorenzo Conti, and Daniela Pietrobon. Defective glutamate and k+ clearance by cortical astrocytes in familial hemiplegic migraine type 2. *EMBO Molecular Medicine*, 8(8):967–986, 2016.

[50] Jun Zhao, Andrew S Blaeser, and Dan Levy. Astrocytes mediate migraine-related intracranial meningeal mechanical hypersensitivity. *Pain*, 162(9):2386, 2021.